Letter

Geometrical control of disorder-induced magnetic domains in planar synthetic antiferromagnets

Kevin Hofhuis [1,2,*] Xueqiao Wang [1,2] Aleš Hrabec [1,2,3] Zhaochu Luo [1,2] Zhentao Liu [1,2] Pietro Gambardella [3] Peter M. Derlet [1,4] and Laura J. Heyderman [1,2,†]

[1]*Laboratory for Mesoscopic Systems, Department of Materials, ETH Zurich, 8093 Zurich, Switzerland*
[2]*Laboratory for Multiscale Materials Experiments, Paul Scherrer Institute, 5232 Villigen PSI, Switzerland*
[3]*Laboratory for Magnetism and Interface Physics, Department of Materials, ETH Zurich, 8093 Zurich, Switzerland*
[4]*Condensed Matter Theory Group, Paul Scherrer Institute, 5232 Villigen PSI, Switzerland*

(Received 20 July 2021; revised 15 November 2021; accepted 11 February 2022; published 4 March 2022)

Magnetic domains play a fundamental role in magnetization processes. However, unlike in ferromagnets (FMs), the formation of domains in antiferromagnets (AFMs) is poorly understood because they are not favored by magnetostatics and are difficult to detect experimentally. In this paper, we create a synthetic planar AFM with tunable lateral coupling between neighboring FM regions to establish the role played by magnetic disorder in the formation of AFM domains. By directly imaging the synthetic AFM in real space, we observe that the AFM lattice spontaneously breaks up into domains following ac demagnetization. These AFM domains nucleate and pin at locally disordered sites that define their size and shape, which is explained with the help of a Gaussian random field Ising model. Furthermore, we can manipulate the AFM domain morphology by varying the interaction strength, which can be tuned with the geometrical parameters of the synthetic AFM.

DOI: 10.1103/PhysRevMaterials.6.L033001

I. INTRODUCTION

Weiss proposed that magnetic materials minimize their free energy by breaking up into magnetic domains separated by magnetic domain walls (DWs) [1]. However, antiferromagnets (AFMs) possess no net magnetization, so that domain formation does not involve the reduction of the magnetostatic energy that leads to the formation of DWs in ferromagnets (FMs). Since such a canonical driving mechanism is absent in AFM systems, and the formation of DWs in AFM systems costs energy, the fundamental origin of AFM domains can be very much material specific. Potential routes to their formation involve a spontaneous magnetic moment formation within the DW [2] or the magnetoelastic effect coupling structural disorder with magnetic disorder [3–5]. In any case, during cooling across the Néel temperature, nucleation of AFM order occurs and is followed by AFM domain formation. Thus, more than a century after Weiss's seminal work [1], the understanding of AFM domain evolution is still in its infancy due to the fact that there are several possible contributions, including magnetostriction, magnetic disorder, entropy, and structural defects, which is further compounded by the notorious difficulty of their detection [6–10]. Understanding the origin of the dominant energetics in AFM domain formation, as well as the structure and interactions of AFM DWs, will allow better control and therefore solve critical issues for optimal data storage densities, memories, and spintronic devices based on AFM materials [8,11–15].

To gain insight into the formation of AFM domains, one can consider artificial spin systems, which are manufactured from mesoscopic magnets. These systems have been developed to study spin-ice physics, and because of their scale, the resulting magnetic structure can be accessed in real space [16,17]. The magnets are often elongated and, because of the ensuing shape anisotropy, attain Ising-like states with the macrospin pointing in one of two directions parallel to the magnet long axis. When placed on various lattices, the macrospins associated with the magnets interact via their long-range stray fields, allowing them to mimic many microscopic phenomena occurring in nature [18–21]. An analogous approach would provide insight into AFM materials, but this has been hindered by a lack of artificial spin systems based solely on a short-ranged nearest-neighbor (NN) AFM coupling [22]. The existence of such short-ranged coupling would open the possibility to create a mesoscopic synthetic AFM that can be visualized using magnetic imaging methods, thereby overcoming the issue with AFM domain detection.

In this paper, we create a planar synthetic AFM that is designed to ascertain the role played by AFM coupling strength and sample disorder in the formation of AFM domains. This is realized utilizing chiral coupling, which arises from the interfacial Dzyaloshinskii-Moriya interaction (DMI) in thin magnetic films [23]. Specifically, we fabricate a planar synthetic AFM consisting of a square lattice of FM regions with tunable AFM coupling between the FM regions that is mediated by the DMI. The role of AFM coupling is taken on by the chiral coupling, and in contrast to dipolar coupled systems [24,25] where further neighbor interactions are important, the interfacial nature of this interaction means that the NN interactions govern the behavior. On the application of an athermal field-driven demagnetization protocol, AFM

*khofhuis@gmail.com
†laura.heyderman@psi.ch

 ©2022 American Physical Society

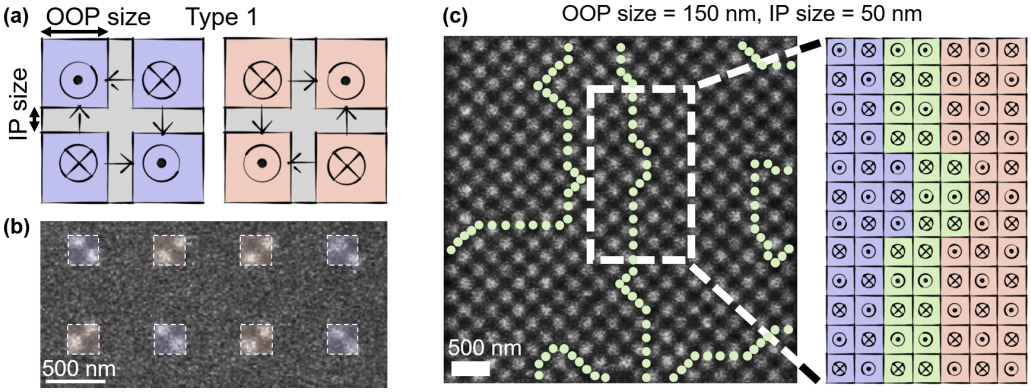

FIG. 1. Planar synthetic antiferromagnets (AFMs). (a) Two degenerate Type 1 AFM building block configurations that follow a left-handed chirality. These states are ensured by the chiral coupling between the nearest-neighbor out-of-plane (OOP) regions mediated via the in-plane (IP) regions. (b) Magnetic force microscopy (MFM) image of individual Type 1 building blocks with the bright and dark contrast indicating up and down OOP magnetizations. (c) MFM image of an extended lattice ($5 \times 5\,\mu m^2$) with the domains comprising building blocks in the Type 1 AFM configuration and domain walls (DWs) separating them (green dots). Zoom-in region shows the spin configuration of two Type 1 domains separated by a DW (green).

domains form whose sizes and structure are controlled by both the coupling strength and the level of disorder. This relation is quantitatively established through the application of the two-dimensional (2D) Gaussian random field Ising model.

II. CONSTRUCTION OF A PLANAR SYNTHETIC AFM

To physically realize such a system, we pattern the magnetic anisotropy of a Pt(6 nm)/Co(1.6 nm)/Al (2 nm) trilayer using local oxidation [26] to define a square lattice of out-of-plane (OOP) magnetized regions ($Pt/Co/AlO_x$) in the in-plane (IP) magnetized (Pt/Co/Al) trilayer (see Supplemental Material (SM) section Sample Preparation [27]). The interfacial DMI arising at the Pt/Co interface induces preferential Néel walls with left-handed chirality in the Co layer that, at the lateral OOP/IP boundary, induces chiral coupling and AFM ordering of the OOP regions [23,28,29]. The resulting effective AFM coupling between adjacent OOP regions is thus mediated by narrow Co regions with IP magnetization that separates the OOP regions (see Fig. 1).

It is useful to consider the building blocks of the system, which consist of four $Pt/Co/AlO_x$ OOP regions and can attain two degenerate lowest-energy configurations obeying left-handed chirality, as shown in Fig. 1(a). This has been experimentally confirmed with magnetic force microscopy (MFM) imaging, as shown in Fig. 1(b). The bright and dark contrast corresponds to up and down OOP magnetizations, while the stray fields associated with the IP Pt/Co/Al regions are too weak to give significant contrast. These doubly degenerate configurations are the basis for the formation of synthetic AFM domains in an extended AFM lattice.

We perform a demagnetization protocol (see SM section Sample Preparation [27]) [30], which results in an AFM domain structure with an example shown in Fig. 1(c). Here, the AFM antiphase domains (in blue and red in the inset) are separated by DWs indicated by green dotted lines. The boundary between the domains, where the relative orientations of the IP and OOP magnetizations are not favored by the chiral coupling, constitutes a synthetic antiphase DW (in green in the inset). Indeed, the two adjacent OOP regions on either side of the DW have magnetizations pointing in the same direction, so forming a collinear AFM order in the form of alternating FM stripes along with the DW. In addition to the collinear DWs running along the two main axes of the square lattice, there can also be parts of DWs that run diagonally and are formed from higher-energy magnetic structures resulting in a faceted AFM DW structure.

III. CHIRAL COUPLING AND MICROMAGNETIC SIMULATIONS OF BUILDING BLOCKS

The DWs that are formed consist of building blocks of four OOP regions with unfavorable magnetization orientation, and to quantify the energy difference between the different configurations, we perform a micromagnetic analysis. There exist four possible building block configurations with different energies associated with them (see SM Fig. S1 [27]). We refer to the lowest energy doubly degenerate configuration as a Type 1 configuration [see also Fig. 1(a)], which forms most of the AFM domains. The Type 2 configuration, with four degenerate states, forms a collinear AFM state within the DWs and has no net magnetization. The energetically unfavorable Type 3 configuration, found in noncollinear DWs, has a net magnetic moment with one OOP region flipped, whereas the Type 4 configuration has all OOP moments pointing in the same direction. Therefore, the DWs consist of the energetically more costly Types 2 and 3 building block configurations with unfavorable IP magnetization orientation between NN OOP regions.

The energy of the building block configurations is determined by simulating the micromagnetic structure using MUMAX3 (v3.10) [31–33]. For this, we obtain the micromagnetic configuration of the four building block types by first setting the associated orientation of the OOP regions and then allowing the IP magnetization to relax (see SM section Micromagnetic Simulations [27]). Assuming a NN dominant interaction [34], the interactions in the micromagnetic simulations are limited to first and second neighbors only.

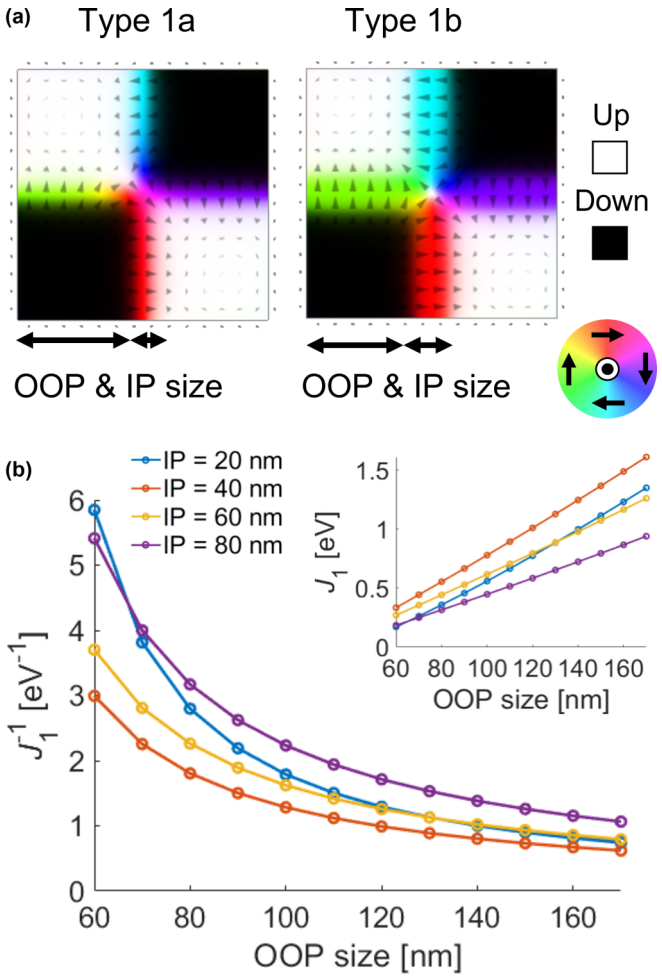

FIG. 2. Micromagnetic simulations of antiferromagnetic (AFM) building blocks. (a) Building block with four out-of-plane (OOP) regions in two low-energy in-plane (IP) configurations denoted Type 1a and Type 1b. The OOP magnetization is given by white/black contrast, and the IP magnetization is given by the color wheel. The central region in the building blocks forms a nontrivial spin texture (Type 1a) for small IP sizes, while for larger IP sizes, an antivortex is formed (Type 1b). (b) A macrospin interaction model is used to extract the trends of the effective AFM nearest-neighbor coupling strength. Both J_1 and the inverse of J_1 is plotted as a function of the OOP and IP dimensions for an IP K_u of 70%.

Interestingly, the DMI coupling between nearest neighbors results in a nontrivial magnetic texture in the IP region at the building block center of the Type 1 configurations [Fig. 2(a)]. Depending on the IP size and the perpendicular magnetic anisotropy (PMA) arising from the Pt/Co interface, either there is an incoherent magnetization [Type 1a in Fig. 2(a)], or an antivortex forms at the center [Type 1b in Fig. 2(a)]. The antivortex is a result of the AFM magnetic ordering and the chiral coupling between OOP regions, which dictates the orientation of the IP magnetization.

These micromagnetic simulations provide an energy for each magnetic configuration. To interpret them in terms of effective interaction strengths between magnetic elements, we employ a macrospin interaction model [35] to estimate the leading-order NN strength of the coupling between the OOP regions J_1 as a function of IP and OOP sizes from the micromagnetic configurations (see SM section Micromagnetic Simulations [27]). We plot the inverse of J_1 in Fig. 2(b) for later comparison with the disorder σ/J_1 that is introduced into the system. As expected, with increasing OOP sizes, the coupling J_1 scales linearly because of the increasing chiral DW length [see inset in Fig. 2(b)]. However, due to the formation of the antivortex, crossovers occur between different IP sizes. In addition, the strongest coupling strengths are seen for an intermediate IP size of 40 nm (for all OOP sizes), in contrast to what one would expect with a leading-order dipolar coupling. Indeed, the dipolar coupling between the OOP elements is an order of magnitude lower than the chiral coupling [29], allowing for the creation and control of a leading-order NN AFM that can be imaged in real space.

IV. SIMULATING THE SYNTHETIC AFM USING THE RANDOM FIELD ISING MODEL

The above simulations motivate the use of a simplified NN interaction Hamiltonian to model the athermal magnetic switching properties of the entire array. Within this framework, we now determine the effect of disorder on the system that, together with the NN interaction, sets the energy scale for the formation of DWs. It should be noted that it is not possible to decouple the underlying simplified Hamiltonian from the disorder. This is because the observed domain structure and its reproducibility on repeating the demagnetization protocol (see SM Fig. S2 [27]) imply that the local critical fields have comparable contributions from both the local coupling and disorder field strengths. To model such a scenario, we consider an OOP macrospin Hamiltonian containing a leading order NN AFM interaction term and a local static effective field representing the underlying local static disorder. Including the applied magnetic field, the effective field may be written as follows:

$$H_{\text{eff}} = J_1 \sum_{i,j>1} \varphi_i \varphi_j + \varphi_i \{H_{\text{ext}} + h_i(\sigma)\}. \tag{1}$$

Here, the first term denotes the macrospins φ defined by the OOP regions with the macrospins either pointing up ($\varphi_i = +1$) or down ($\varphi_i = -1$). Also, J_1 is the NN AFM coupling, the second term is associated with the external field H_{ext} that drives the system, and disorder is included with an additional local random OOP field term $h_i(\sigma)$ for each OOP macrospin. The magnitude of the local random field at each site is sampled using a Gaussian distribution with a standard deviation σ, whose value can be viewed as a measure of the strength of the disorder within the system. We assume that such a simplified disorder suitably characterizes the real disorder originating from structural (and therefore magnetic) variations in the experimental system. A stable magnetic configuration occurs when all OOP macrospins are aligned with their local effective fields ($H_{\text{eff}} = -\frac{dH}{d\varphi_i}$, which are positive). Upon application of an external field, athermal local reorientation of the ith OOP macrospin will occur when H_{eff} becomes negative. In this way, athermal reorientation of a spin will depend on the energetics of the four NN spin configurations as well as the underlying disorder through the effective local static field. This defines the well-known Gaussian random

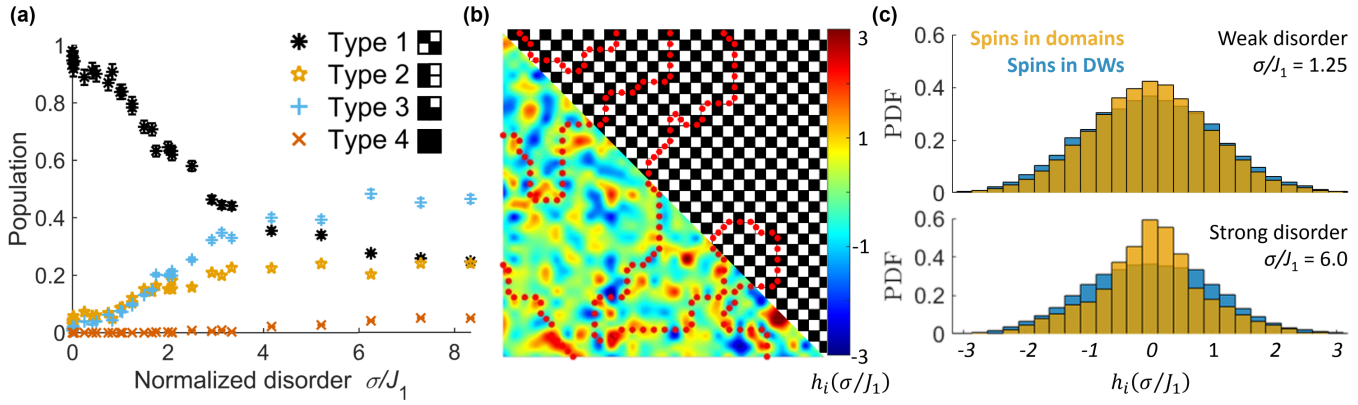

FIG. 3. Simulations using the macrospin model with disorder. (a) Simulated population of configuration types as a function of the introduced disorder σ/J_1 normalized to the nearest-neighbor (NN) coupling strength J_1 after a demagnetization protocol. An average is taken from 10 random realizations of disorder, and it is found that the number of domain walls (DWs) consisting of energy-costly Type 2 and 3 configurations increases with disorder. The crossing from weak to strong disorder is at $\sigma/J_1 = 4$. (b) Final antiferromagnetic (AFM) domain configuration derived from a 31 × 31 macrospin simulation with ($\sigma/J_1 = 1.25$), where the white and black out-of-plane (OOP) regions denote up and down spins, and the DWs are indicated with red dots. The spatial disorder $h_i(\sigma/J_1)$ is plotted as a color code, with the pinning of DWs (red dots) at the high disorder sites. (c) Simulated probability distribution functions (PDFs) of spins for a particular disorder (h_i) in the domains (in yellow) and in the DWs (in blue). The top graph is for weak disorder ($\sigma/J_1 = 1.25$), and the bottom graph is for strong disorder ($\sigma/J_1 = 6.0$). From this, we can conclude that pinning of DWs occurs at the higher disorder sites (see explanation in the main text).

field model, which is often used to model FM materials and exchange biased AFM/FM materials [36–40].

To determine the strength of disorder in our experimental systems, we first simulated an open boundary system of 31 × 31 spins undergoing a field demagnetization protocol like the field protocol used in our experiments (see SM section Macrospin Simulations [27]). During the simulated demagnetization protocol, domains are nucleated at sites with large local random fields. The population of configuration types as a function of the introduced disorder σ/J_1, normalized to the NN coupling strength J_1, are plotted in Fig. 3(a) following a simulated demagnetization protocol. The crossing from weak to strong disorder occurs at $\sigma/J_1 = 4$ in Fig. 3(a), when the population of Type 3 configurations becomes greater than twice the population of Type 2 configurations, considering that the degeneracy of the Type 3 building block is twice that of the Type 2 building block ($\mathrm{DEG}_{\mathrm{Type2}} = 4$, $\mathrm{DEG}_{\mathrm{Type3}} = 8$, see SM Fig. S1 [27]). For weak disorder ($\sigma/J_1 < 4$), magnetic switching usually manifests itself as a system-spanning avalanche of neighboring spins flipping their magnetization so that the nucleated domain expands throughout the system via propagation of collinear DWs that are along the principal direction of the underlying lattice and are constructed mainly of Type 2 configurations (see SM Video 1 [27]). In contrast, for a strong disorder ($\sigma/J_1 > 4$), such avalanches are often arrested due to pinning, resulting in the simultaneous existence of many small domains and a more complex evolution of noncollinear, staggered DWs that consist of higher-energy Type 3 configurations (see SM Video 2 [27]).

V. QUANTIFICATION OF EXPERIMENTAL DISORDER AND ITS ROLE IN AFM DOMAIN FORMATION

Through detailed inspection of the simulated spin configurations, one finds that the locations of the DWs correlate with the corresponding spatial distribution of the disorder [see Fig. 3(b)]. We find that short segments of the DW are located at sites where the local random field has a large magnitude. The normalized probability density function (PDF) of the disorder fields (h_i) for spins located within the domain (yellow distribution) or the DW (blue distribution) are shown in Fig. 3(c) for both weak disorder (top) and strong disorder (bottom). Comparing the strong disorder case with the weak disorder case, there is an increased probability to find higher disordered spins $h_i(|\sigma|) > 1$ as part of the DWs, indicated by the broader blue curve, while the probability at $h_i = 0$ for spins in the domain increases for strong disorder indicated by the sharper peak in yellow. In addition, if a site has an extremal value of field magnitude, defined as $h_i > 2\sigma$, then the probability that it is a DW segment is 15% more likely than the global average. Hence, we can conclude that pinning of DWs occurs at the higher disorder sites, and since there are more sites with high disorder present in the strong disorder sample, there are more domain boundaries and smaller domains. It should also be pointed out that, like what is seen in the experiment, after applying several demagnetization protocols, it is found that a particular realization of the disorder will result in the same magnetic structure. Moreover, the simulated final demagnetized AFM state is comparable with what we have seen in the experiment. The experimental domain structure shown in Fig. 1(c) consists mainly of collinear DWs, allowing us to conclude that this experimental system corresponds to an example of weak disorder.

Experimentally, we can control the degree of normalized disorder (σ/J_1) by varying both the OOP and IP size. To quantitatively investigate the role of disorder, we fabricated lattices with the OOP sizes ranging from 75 to 150 nm in steps of 25 nm. At each OOP size, we vary the IP size from 40 to 80 nm in steps of 20 nm. The final magnetic configurations following application of the demagnetization protocol (see SM section Sample Preparation [27]) are measured using MFM to obtain

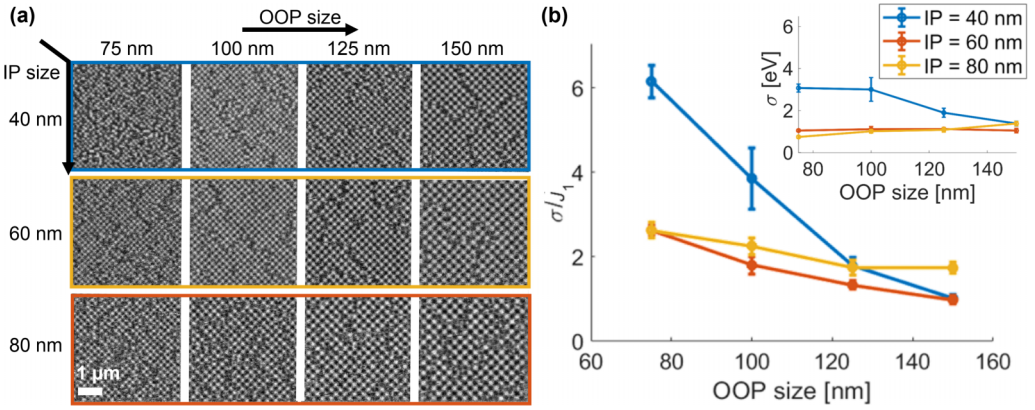

FIG. 4. Control of antiferromagnetic domain size through geometry. (a) Magnetic force microscopy (MFM) images taken from $5 \times 5\ \mu m^2$ arrays with various out-of-plane (OOP) and in-plane (IP) sizes after applying the demagnetization protocol to the 12 different arrays, which are repeated five times on the sample. All arrays are measured to increase sample statistics. The resulting OOP spin configurations are extracted from the MFM images, and we determine the average populations of configuration types for each geometry. (b) These experimental populations are least-square fitted to the Monte Carlo results from Fig. 3(a) to obtain an estimate of the disorder σ/J_1. The largest domain sizes, corresponding to the lowest disorder, are found for a system with an intermediate IP size of 40 to 60 nm and an OOP size of 150 nm. This result of an intermediate IP size corresponding to the strongest coupling is like the results obtained from micromagnetic simulations. In the inset, the disorder strength σ is determined using J_1 from micromagnetic simulations [Fig. 2(b) inset]. The disorder is found to be (qualitatively) constant for IP sizes of 60 and 80 nm, while the smallest size of IP = 40 nm shows an increasing disorder with decreasing OOP size.

the phase-contrast found in Fig. 4(a), where it can immediately be seen that, as the OOP size increases, the domain size increases. To obtain statistically meaningful information, five different arrays for each OOP and IP size are manufactured, allowing for the averaging over the underlying disorder. To obtain a quantitative measure of disorder, we perform a least-squares fit of the populations in our experimental system to the simulated disorder model populations in Fig. 3(a). In this way, we determine a representative value of σ/J_1 for the various experimental systems with different OOP and IP, and this is given in Fig. 4(b). In the inset of Fig. 4(b), we used the J_1 from micromagnetic simulations to determine the disorder strength (σ) and find that, for IP sizes of 60 and 80 nm, σ is constant for all OOP sizes. However, for the smallest IP size of 40 nm, there is an increase in disorder for decreasing OOP size, which is likely to be the result of the increased importance of lithographic irregularities for smaller feature sizes. The fact that the disorder σ/J_1 decreases with OOP size in Fig. 4(b), while the disorder strength σ is nearly constant, confirms that the coupling strength J_1 increases with OOP size, as seen in the inset of Fig. 2(b). The decrease in σ/J_1 also leads to an increase in AFM domain size, as reflected by the increase in Type 1 building block population seen in Fig. 3(a). Therefore, the increased coupling strength reduces the effect disorder has on the final AFM domain structure. Furthermore, crossovers between different IP sizes are found that are likely to be due to the formation of the different structures (Type 1a and 1b) in the IP region, as was observed from our analysis of the micromagnetic simulations in Fig. 2. Experimentally, we find an optimum IP size of 40 to 60 nm for the strongest coupling, at which the AFM domains are largest [see Fig. 4(b)]. By fitting the MFM data shown in Fig. 4(a) to the simulated populations [Fig. 3(a)], we have shown that a model Hamiltonian can be used to characterize the formation of AFM domains by DW pinning due to disorder [Fig. 4(b)], allowing us to conclude that the AFM domain structural length scales are controlled by both intrinsic disorder and the magnitude of the NN AFM interaction. Given that disorder is always present, we have opened the way to control the desired length scale that characterizes the AFM domains by fine-tuning the dimensions of the system to engineer an optimal NN AFM interaction.

VI. SUMMARY AND OUTLOOK

We demonstrate that synthetic AFMs with tunable coupling strengths are exemplary candidates for the understanding of AFM domain formation and the role of disorder. With the help of micromagnetic simulations, the nontrivial dependence of the effective NN AFM coupling J_1 on the size of the IP magnetized regions is explained by antivortex formation in the central IP regions. We demonstrate that the pinning of DWs in regions of high disorder is the driving mechanism for AFM domain formation, and through a local Gaussian random field Ising model characterized by a disorder width σ, the deterministic domain formation in our synthetic AFM is found to be intimately related to the level of disorder and the strength of the AFM coupling through the ratio σ/J_1. For the observed range $1 < \sigma/J_1 < 6$, we see different complex behavior that depends on the level of disorder. At weak disorder ($\sigma/J_1 < 4$), we find a collinear DW regime with the walls made up of Type 2 building blocks, while for strong disorder ($\sigma/J_1 > 4$), we find small domains (indicated by the low Type 1 populations) with DWs made up of Type 3 building blocks. The calculated disorder σ using the J_1 from micromagnetic simulations is found to be constant for the IP sizes 60 and 80 nm, while for the smallest IP size of 40 nm, there is an increasing disorder with decreasing OOP size. This is likely due to the increased importance of irregularities resulting from the lithographic processes at very small feature sizes.

In this paper, we have created synthetic AFM structures that can be imaged in real space, thus overcoming the difficulties involved in imaging microscopic AFMs. Furthermore, this gives the possibility to observe avalanche dynamics [40] in AFMs using magneto-optic Kerr effect microscopy [24]. More generally, we demonstrate that we can control synthetic AFM domain structures by tuning the relative interaction strength through altering the geometry. In addition, tailor-made disorder can be introduced into synthetic AFMs using ion gating [41] and helium irradiation [42]. While in this paper we provide an insight into the role of disorder and pinning in the formation of synthetic AFM domains for a square-lattice AFM, the presented approach can be extended to other synthetic AFMs arranged, for example, on Archimedean lattices [43]. Here, other effects can be systematically studied in real space, such as thermal dynamics, disorder-induced spin-glass behavior, and several other fascinating phenomena in frustrated lattices including spin-ice or spin-liquid behavior.

All data generated and analyzed during this study are available via the Zenodo repository [44].

ACKNOWLEDGMENTS

This paper was supported by the Swiss National Science Foundation Project 200020_172774 and 200021_182013. A.H. was funded by the European Union's Horizon 2020 research and innovation program under Marie Skłodowska-Curie Grant Agreement No. 794207 (ASIQS). X.W. acknowledges the ThinkSwiss Research Scholarship.

K.H. and A.H. conceived the experiments, and X.W. and Z.Liu assisted in the measurements. Z.Luo and X.W. contributed to sample preparation. K.H. derived the models and analyzed the data. All authors discussed the results and contributed to the final paper.

Authors declare no competing interests.

[1] P. Weiss, La variation du ferromagnetisme du temperature, Comptes Rendus **143**, 1136 (2009).

[2] N. Papanicolaou, Antiferromagnetic domain walls, Phys. Rev. B **51**, 15062 (1995).

[3] W. L. Roth, Neutron and optical studies of domains in NiO, J. Appl. Phys. **31**, 2000 (1960).

[4] H. Gomonay and V. M. Loktev, Magnetostriction and magnetoelastic domains in antiferromagnets, J. Phys. Condens. Matter **14**, 3959 (2002).

[5] H. V. Gomonay and V. M. Loktev, Shape-induced phenomena in finite-size antiferromagnets, Phys. Rev. B **75**, 174439 (2007).

[6] A. Scholl, Observation of antiferromagnetic domains in epitaxial thin films, Science **287**, 1014 (2000).

[7] H. Ohldag, A. Scholl, F. Nolting, S. Anders, F. U. Hillebrecht, and J. Stöhr, Spin Reorientation at the Antiferromagnetic NiO(001) Surface in Response to an Adjacent Ferromagnet, Phys. Rev. Lett. **86**, 2878 (2001).

[8] M. S. Wörnle, P. Welter, Z. Kašpar, K. Olejník, V. Novák, R. P. Campion, P. Wadley, T. Jungwirth, C. L. Degen, and P. Gambardella, Current-induced fragmentation of antiferromagnetic domains, arXiv:1912.05287.

[9] S. W. Cheong, M. Fiebig, W. Wu, L. Chapon, and V. Kiryukhin, Seeing is believing: visualization of antiferromagnetic domains, Npj Quantum Mater. **5**, 3 (2020).

[10] N. Hedrich, K. Wagner, O. V. Pylypovskyi, B. J. Shields, T. Kosub, D. D. Sheka, D. Makarov, and P. Maletinsky, Nanoscale mechanics of antiferromagnetic domain walls, Nat. Phys. **17**, 574 (2021).

[11] A. N. Lavrov, S. Komiya, and Y. Ando, Magnetic shape-memory effects in a crystal, Nature (London) **418**, 385 (2002).

[12] A. V. Goltsev, R. V. Pisarev, T. Lottermoser, and M. Fiebig, Structure and Interaction of Antiferromagnetic Domain Walls in Hexagonal $YMnO_3$, Phys. Rev. Lett. **90**, 177204 (2003).

[13] P. Wadley, B. Howells, J. Železný, C. Andrews, V. Hills, R. P. Campion, V. Novák, K. Olejník, F. Maccherozzi, S. S. Dhesi, S. Y. Martin, T. Wagner, J. Wunderlich, F. Freimuth, Y. Mokrousov, J. Kuneš, J. S. Chauhan, M. J. Grzybowski, A. W. Rushforth, K. Edmond *et al.*, Electrical switching of an antiferromagnet, Science **351**, 587 (2016).

[14] S. Y. Bodnar, L. Šmejkal, I. Turek, T. Jungwirth, O. Gomonay, J. Sinova, A. A. Sapozhnik, H. J. Elmers, M. Klaüi, and M. Jourdan, Writing and reading antiferromagnetic Mn_2Au by Néel spin-orbit torques and large anisotropic magnetoresistance, Nat. Commun. **9**, 348 (2018).

[15] F. Schreiber, L. Baldrati, C. Schmitt, R. Ramos, E. Saitoh, R. Lebrun, and M. Kläui, Concurrent magneto-optical imaging and magneto-transport readout of electrical switching of insulating antiferromagnetic thin films, Appl. Phys. Lett. **117**, 082401 (2020).

[16] R. F. Wang, C. Nisoli, R. S. Freitas, J. Li, W. McConville, B. J. Cooley, M. S. Lund, N. Samarth, C. Leighton, V. H. Crespi, and P. Schiffer, Artificial 'spin ice' in a geometrically frustrated lattice of nanoscale ferromagnetic islands, Nature (London) **439**, 303 (2006).

[17] S. H. Skjærvø, C. H. Marrows, R. L. Stamps, and L. J. Heyderman, Advances in artificial spin ice, Nat. Rev. Phys. **2**, 13 (2020).

[18] G. Möller and R. Moessner, Artificial Square Ice and Related Dipolar Nanoarrays, Phys. Rev. Lett. **96**, 237202 (2006).

[19] Y. Lao, F. Caravelli, M. Sheikh, J. Sklenar, D. Gardeazabal, J. D. Watts, A. M. Albrecht, A. Scholl, K. Dahmen, C. Nisoli, and P. Schiffer, Classical topological order in the kinetics of artificial spin ice, Nat. Phys. **14**, 723 (2018).

[20] D. Shi, Z. Budrikis, A. Stein, S. A. Morley, P. D. Olmsted, G. Burnell, and C. H. Marrows, Frustration and thermalization in an artificial magnetic quasicrystal, Nat. Phys. **14**, 309 (2018).

[21] N. Rougemaille and B. Canals, Cooperative magnetic phenomena in artificial spin systems: spin liquids, coulomb phase and fragmentation of magnetism—a colloquium, Eur. Phys. J. B **92**, 62 (2019).

[22] Y. Perrin, B. Canals, and N. Rougemaille, Extensive degeneracy, coulomb phase and magnetic monopoles in artificial square ice, Nature (London) **540**, 410 (2016).

[23] Z. Luo, T. P. Dao, A. Hrabec, J. Vijayakumar, A. Kleibert, M. Baumgartner, E. Kirk, J. Cui, T. Savchenko, G. Krishnaswamy,

L. J. Heyderman, and P. Gambardella, Chirally coupled nanomagnets, Science **363**, 1435 (2019).

[24] S. Kempinger, R. D. Fraleigh, P. E. Lammert, S. Zhang, V. H. Crespi, P. Schiffer, and N. Samarth, Imaging the stochastic microstructure and dynamic development of correlations in perpendicular artificial spin ice, Phys. Rev. Research **2**, 012001(R) (2020).

[25] S. Kempinger, Y. S. Huang, P. E. Lammert, M. Vogel, A. Hoffmann, V. H. Crespi, P. Schiffer, N. Samarth, R. D. Fraleigh, P. E. Lammert, S. Zhang, V. H. Crespi, P. Schiffer, N. Samarth, K. M. McPeak, S. V. Jayanti, S. J. P. Kress, S. Meyer, S. Iotti, A. Rossinelli *et al.*, Field-Tunable Interactions and Frustration in Underlayer-Mediated Artificial Spin Ice, Phys. Rev. Lett. **127**, 117203 (2020).

[26] S. Monso, B. Rodmacq, S. Auffret, G. Casali, F. Fettar, B. Gilles, B. Dieny, and P. Boyer, Crossover from in-plane to perpendicular anisotropy in Pt/CoFe/AlO_x sandwiches as a function of Al oxidation: A very accurate control of the oxidation of tunnel barriers, Appl. Phys. Lett. **80**, 4157 (2002).

[27] See Supplemental Material at http://link.aps.org/supplemental/10.1103/PhysRevMaterials.6.L033001 for details on micromagnetic and macrospin simulations, as well as the sample preparation.

[28] O. Boulle, J. Vogel, H. Yang, S. Pizzini, D. De Souza Chaves, A. Locatelli, T. O. Menteş, A. Sala, L. D. Buda-Prejbeanu, O. Klein, M. Belmeguenai, Y. Roussigné, A. Stashkevich, S. Mourad Chérif, L. Aballe, M. Foerster, M. Chshiev, S. Auffret, I. M. Miron, and G. Gaudin, Room-temperature chiral magnetic skyrmions in ultrathin magnetic nanostructures, Nat. Nanotechnol. **11**, 449 (2016).

[29] A. Hrabec, Z. Luo, L. J. Heyderman, and P. Gambardella, Synthetic chiral magnets promoted by the Dzyaloshinskii-Moriya interaction, Appl. Phys. Lett. **117**, 130503 (2020).

[30] R. F. Wang, J. Li, W. McConville, C. Nisoli, X. Ke, J. W. Freeland, V. Rose, M. Grimsditch, P. Lammert, V. H. Crespi, and P. Schiffer, Demagnetization protocols for frustrated interacting nanomagnet arrays, J. Appl. Phys. **101**, 09J104 (2007).

[31] A. Vansteenkiste, J. Leliaert, M. Dvornik, M. Helsen, F. Garcia-Sanchez, and B. Van Waeyenberge, The design and verification of MUMAX3, AIP Adv. **4**, 107133 (2014).

[32] J. Mulkers, B. Van Waeyenberge, and M. V. Milošević, Effects of spatially engineered Dzyaloshinskii-Moriya interaction in ferromagnetic films, Phys. Rev. B **95**, 144401 (2017).

[33] J. Leliaert, M. Dvornik, J. Mulkers, J. De Clercq, and M. V. Milo, Fast micromagnetic simulations on GPU—recent advances made with MUMAX3, J. Phys. D Appl. Phys. **51**, 123002 (2018).

[34] J. Colbois, K. Hofhuis, Z. Luo, X. Wang, A. Hrabec, L. J. Heyderman, and F. Mila, Artificial out-of-plane Ising antiferromagnet on the kagome lattice with very small farther-neighbor couplings, Phys. Rev. B **104**, 024418 (2021).

[35] X. N. Wu, Exact results for lattice models with pair and triplet interactions, J. Phys. A. Math. Gen. **22**, L1031 (1989).

[36] O. Perković, K. Dahmen, and J. P. Sethna, Avalanches, Barkhausen Noise, and Plain Old Criticality, Phys. Rev. Lett. **75**, 4528 (1995).

[37] O. Perković, K. A. Dahmen, and J. P. Sethna, Disorder-induced critical phenomena in hysteresis: Numerical scaling in three and higher dimensions, Phys. Rev. B **59**, 6106 (1999).

[38] B. Koiller and M. O. Robbins, Morphology transitions in three-dimensional domain growth with Gaussian random fields, Phys. Rev. B **62**, 5771 (2000).

[39] A. Berger, A. Inomata, J. S. Jiang, J. E. Pearson, and S. D. Bader, Experimental Observation of Disorder-Driven Hysteresis-Loop Criticality, Phys. Rev. Lett. **85**, 4176 (2000).

[40] J. P. Sethna, K. A. Dahmen, and C. R. Myers, Crackling noise, Nature (London) **410**, 242 (2001).

[41] U. Bauer, L. Yao, A. J. Tan, P. Agrawal, S. Emori, H. L. Tuller, S. Van Dijken, and G. S. D. Beach, Magneto-ionic control of interfacial magnetism, Nat. Mater. **14**, 174 (2015).

[42] M. V. Sapozhnikov, S. N. Vdovichev, O. L. Ermolaeva, N. S. Gusev, A. A. Fraerman, S. A. Gusev, and Y. V. Petrov, Artificial dense lattice of magnetic bubbles, Appl. Phys. Lett. **109**, 042406 (2016).

[43] U. Yu, Ising antiferromagnet on the Archimedean lattices, Phys. Rev. E **91**, 062121 (2015).

[44] https://doi.org/10.5281/zenodo.6092452.